Stability and Activity Controls of Cu Nanoparticles for High-performance Solid Oxide Fuel Cells

Seungyeon Jo[a]*, HyeonGwon Jeong*[a]*, Yo Han Kim*[a]*, Dragos Neagu*[b]* and Jae-ha Myung*[a]*

[a]Department of Materials Science and Engineering, Incheon National University, Incheon 22012, Korea

[b]Department of Chemical and Process Engineering, University of Strathclyde, Glasgow, G1 1XL, UK

[*]Corresponding authors.

E-mail addresses: mjaeha@inu.ac.kr (J. Myung), dragos.neagu@strath.ac.uk (D. Neagu)

KEYWORDS

Solid oxide fuel cell, in-situ exsolution, Cu nanoparticles, infiltration, thermal stability

ABSTRACT

Cu-based electrodes could advance solid oxide fuel cells (SOFC) technology due to good electric conductivity and relatively high electrochemical activity among transition metals. However, one

of the main challenges for designing anode materials is thermal stability in SOFC operation condition. Herein, a promising anode material decorated with Cu nanoparticles (NPs) was synthesized via in-situ exsolution from $La_{0.43}Sr_{0.37}Cu_{0.12}Ti_{0.88}O_{3-\delta}$ (LSCuT) perovskite. Compared to infiltration process, Cu NPs prepared by in-situ exsolution displayed homogeneous nano size distribution on the substrate and excellent thermal stability at 600 °C in H_2 atmosphere, for ~50 h. In addition, we employed electrochemical reduction (ER) at 2.3 volts for a few seconds to demonstrate that NPs can be rapidly grown, and the substrate reduced. A single cell with LSCuT anode (10 μm)‖ScSZ electrolyte (90 μm) ‖LSM-ScSZ cathode (20 μm) exhibits maximum power density of 1.38 Wcm^{-2} at 900 °C under wet H_2. The present study provides possibility of a broad application of thermally stable Cu-based electrodes.

1. Introduction

Solid oxide fuel cells (SOFC) are promising power generators, allowing to directly convert chemical energy to electricity with low emission and high efficiency, making it a be major clean energy conversion technology in the future[1,2.] However, there are limitations to be overcomed in the commercialization of SOFC, primarily due to lack of optimal anode materials for high temperature operation (600-900 °C), the region where efficiency is maximized. Even though the conventional Ni based cermet anode has high catalytic activity and electrical conductivity at high temperature, it also suffers from rapid performance degradation because of low tolerance to redox cycle, and agglomeration of the metal phase during prolonged usage[3,4]. Therefore, designing thermally stable anodes is one of the main challenges to address for SOFC electrode applications[5]. To overcome the stability limitations of anode materials in high temperature operation, recent

2

R&D has concentrated on developing perovskite electrodes in conjunction with 'in-situ exsolution' where the metal NPs are socketed and thus better anchored into perovskite structure oxides (ABO_3)[6,7,8,9,10]. Perovskite oxides are employed as porous backbone for the electrode due to their capability to display mixed ionic and electronic conductivity, while maintaining stability in redox conditions[11]. To exsolve metal nanoparticles, reducible metal cations are doped at the B-site, which can additionally promote catalytic activity of the materials[12,13]. In addition, introducing point defects through A-site and O-site non-stoichiometry (typically deficiency) maximizes the exsolution phenomenon[14]. Non-stoichiometry can be achieved through hetero-doping and implicit charge compensation, for example substituting Sr^{2+} by La^{3+} in $SrTiO_3$ leads to non-stoichiometry, $Sr_{1-3x/2}La_xTiO_3$, which promotes B-site exsolution under reduction[8].

Although the conventional method of infiltration is widely used to introduce the catalyst on the electrode surface[15,16], it often leads to subsequent degradation by agglomeration over time, during operation, at high temperatures. Moreover, infiltration requires multiple cycles of impregnation and thermal treatment that are time-consuming and which also limits NP size control and bonding with the scaffold[5,17]. Compared to infiltration process, exsolved metal NPs such as Ni[18,19], Fe[20,21], Co[22] and alloy[23,24] not only display high catalytic activity, but also exhibit lower propensity for agglomeration even at high temperatures because of the strong interaction between NP and the oxide surface. Until now, in-situ exsolved NPs decorated perovskite systems, such as $La_{0.43}Ca_{0.37}Ni_{0.06}Ti_{0.94}O_{3-\delta}$[18], $La_{0.2}Sr_{0.7}Ti_{0.9}Ni_{0.1}O_{3-\delta}$[25], $La_{0.5}Sr_{0.5}Fe_{0.9}Nb_{0.1}O_{3-\delta}$[26], $La_{0.6}Sr_{0.4}Co_{0.7}Mn_{0.3}O_3$[27] and $La_{0.5}Sr_{0.5}Co_{0.45}Fe_{0.45}Nb_{0.1}O_{3-\delta}$[28] have been used as sole anode materials and have shown excellent catalytic activity and stability compared with conventional processed materials. However, there are few studies on Cu based materials because of its low melting temperature (1083 °C) and high mobility[29]. The low melting temperature causes loss of

active sites because of agglomeration of NPs at high temperature[30,31]. In this article, we demonstrate that these issues can be alleviated by applying the exsolution process. In addition, Cu is a good catalyst for SOFC anode, and it also improves their electronic conductivity[32]. Cu-based oxides can also lower the sintering temperature of perovskite materials which is usually synthesized at high temperature (>1300 °C)[22,33,34].

In this work, we designed $La_{0.43}Sr_{0.37}Cu_{0.12}Ti_{0.88}O_{3-\delta}$ (LSCuT) perovskite capable of exsolving homogenous Cu NPs. A-site deficiency (A/B<1) was introduced to promote exsolution from the B-site , by improving the reducibility and diffusion of oxide ions and cations, as shown previously, leading additionally to enhanced mixed ionic and electronic conductivity by forming more oxygen vacancies[17,35,36]. We benchmark our results against an analogous system, $La_{0.43}Sr_{0.37}TiO_{3-\delta}$ (LST) which we infiltrated with an amount of Cu equivalent to that in the doped/exsolved perovskite (12 mol% doping/loading). The synthesized material is a promising anode catalyst for SOFC in terms of stability and electrochemical performance. Compared to the infiltration process, exsolved Cu shows that our materials have excellent thermal stability in dry H_2 gas at 600 °C for ~50 h. This material was used as anode in ScSZ electrolyte supported SOFC cells. The cells display exceptional performance with electrochemical reduction, which can produce emergent NPs on the substrate.

2. Experimental

2.1. Materials Preparation

$La_{0.43}Sr_{0.37}Cu_{0.12}Ti_{0.88}O_{3-\delta}$ and $La_{0.43}Sr_{0.37}TiO_{3-\delta}$ (serving as undoped, benchmark material and support for infiltration comparison) powder were prepared using a solid-state reaction process[37]. Stoichiometric amounts of La_2O_3 (99.9 %, Alfa aesar), $SrCO_3$ (99.9 %, Sigma-Aldrich), CuO

(Sigma) and TiO$_2$ (99.8 %, Sigma-Aldrich) were mixed with ethanol by stirring for 24 h. Subsequently, the mixture was evaporated at 80 °C to form a precursor mixture. The resultant powders were subjected to calcination at 1000 °C for 3 h to decompose the carbonates and start phase nucleation. The calcined powders were uniaxially pressed into pellets with 25.4 mm diameter and then finally sintered at 1200 °C for 10 h to obtain a single-phase perovskite. The structural characterization of prepared samples was conducted by a Rigaku SmartLab X-ray diffraction (XRD) with Rietveld refinement method over the range of 20~80° with Cu K$_\alpha$ radiation (scanning rate was 6° min^{-1}). To exsolve nanoparticles on the perovskite surface, the reduction was carried out in a pure H$_2$ at various temperature (400 to 700 °C) and time (12 to 36 h).

2.2 Cell fabrication and morphological analysis

The ScSZ electrolyte support with a thickness 90 µm was prepared by tape-casting method. The ScSZ powder, commercial binder solution (B74001, Ferro, USA) and dibutyl phthalate (DBP) were added and ball-milled for 24 h. The wight ratio of the mixtures (ScSZ powder and binder solution) was 50 : 50. The ScSZ tape was cast onto a heated plate (45 °C) and the tape thickness was controlled by the height of the doctor blade (400 µm). The thickness of the green tapes was 110 µm. The green tape cut into disks, and then sintered at 1450 °C 6 h. Samples for electrochemical test were prepared by conventional screen-printing method. LSCuT and LST perovskite materials were mixed with organic binder (α-terpineol and ethyl cellulose) and high energy milled for 15 min to make viscous paste, respectively. Cathode electrode of (La$_{0.80}$Sr$_{0.20}$)$_{0.95}$MnO$_{3-\delta}$ (LSM)-(Sc$_2$O$_3$)$_{0.10}$(CeO$_2$)$_{0.01}$(ZrO$_2$)$_{0.89}$ (ScSZ) paste in weight ratio of 5:5 was also prepared by the same process mentioned above. Each paste was screen printed on the both side of thin ScSZ (~90 µm) electrolyte support and sintered at 1050 °C for 3 h to obtain porous

electrode layer. The active surface area of each electrode was determined to be 0.5 cm^2. Infiltration process was employed on porous LST electrode layer by using a Cu nitrate aqueous solution. The concentration of urea in the precursor solution was 10 times higher than that of Cu ions, to ensure enough dispersion and formation of Cu nanoparticles on the LST electrode surface[38,39,40]. Thermal treatment was conducted at 80 °C for 2 h to decompose urea and calcined at 400 °C for 2 h to eliminate organic compounds. The amount of Cu ions used for both infiltration and exsolution process were fixed to be 12 mol% compared with LSCuT perovskite mother phase for catalytic comparison.

The morphological analysis of two different electrode structures was conducted after reduction using dry H$_2$. The reduction was conducted at 600 °C at various times, ranging from 12 to 48 h. The Cu nano particles on the perovskite surface were investigated using a JEOL JSM-7001F scanning electron microscope (SEM) and the resulting images binarized and analyzed using image J software. The chemical distribution of perovskite and Cu nano particles were analyzed by a FEI TALOS F200X transmission electron microscope equipped with energy dispersive X-ray spectroscopy (TEM-EDS).

2.3. Electrochemical properties and reducibility test

The reducibility of LSCuT and LST were characterized by H$_2$-temperature programmed reduction (H$_2$-TPR). Samples of 70 mg were pre-heated in He up to 300 °C for 2 h. After cooling, the powders were exposed to 10 % H$_2$/Ar (10 mL/min) from room temperature to 900 °C.

The prepared button cells were sealed by Pyrex glass sealants and mounted on an alumina jig. Pt mesh and paste were attached on the both side of electrode surface for proper current collection. The gas control system included gas mass flow controllers for N$_2$ and H$_2$, liquid flow meter for

H$_2$O and controlled evaporator mixer for supplying steam H$_2$O using N$_2$ gas (50 % H$_2$O/N$_2$). Electrochemical reduction before cell test was carried out by applying 2.3 V (versus air electrode) for ~100 seconds at 900 °C under 50 % H$_2$O/N$_2$ atmosphere. After reduction, the gas atmosphere for anode electrode was changed to 3 % H$_2$O/H$_2$ for fuel cell operation test. The schematic illustration of the cell operating condition is shown in Fig. S1. Electrochemical tests were conducted using a VMP-300 potentiostat. Linear sweep voltammetry (LSV) was conducted to evaluate peak power density of each sample. Electrochemical impedance spectroscopy (EIS) method was conducted to investigate the characteristic impedance of each electrode design. Nyquist plots were recorded at open circuit voltage (OCV) conditions with frequency range from 100 kHz to 100 mHz. The amplitude was determined to 30 mV for clear impedance spectra of regarding electrochemical reactions.

3. Results and discussion

3.1. Characterization of catalysts

The crystal structure of the materials before and after reduction was investigated using XRD as shown in Fig. 1a and Fig. S2a. The La$_{0.43}$Sr$_{0.37}$TiO$_{3-\delta}$ (LST) and La$_{0.43}$Sr$_{0.37}$Cu$_{0.12}$Ti$_{0.88}$O$_{3-\delta}$ (LSCuT) samples exhibit a perovskite structure without secondary phases. The crystal structure of oxidized sample was refined by Rietveld analysis of the XRD results (Fig. S3). The LSCuT phase has a Rhombohedral crystal structure with a R-3c space group. The weighted profile R-factor (R$_{wp}$) values for LSCuT is 0.05, indicating that the refinement results were reliable and confirm phase purity. The diffraction peak of LSCuT shifted toward lower angles, as compared to the undoped LST, as shown in fig. S2b. This observation suggest that the unit cell volume increased with the

Cu substitution (ionic radii: $Ti^{4+} = 0.605$ Å, $Cu^{2+} = 0.73$ Å), confirming successful substitution of Cu without secondary phases.

Upon subjecting LSCuT to reducing atmosphere (dry H_2), at various temperatures (400 to 700 °C) for 12 h, diffraction peaks associated with metal Cu became apparent, as shown in Fig. 1a (inset graph shows Cu main peaks). Nonetheless, the samples retain their perovskite phase at all temperatures. It is worth noting that Cu was exsolved from the perovskite oxide at temperatures as low as 400 °C. To verify the reducibility of Cu ions in the perovskite, H_2-TPR analysis were investigated on LSCuT and LST (Fig. S4a). The LST sample displays no obvious peak during the measurement. However, the LSCuT sample has a main peak at a temperature of ~200 °C, which we assign to the reduction of Cu^{2+} to Cu^0. As shown in Fig. 1a, it was confirmed that there was no CuO peaks as a secondary phase, which suggests that the Cu was successfully doped in the perovskite lattice. Therefore, these results indicate that Cu can exsolve from the perovskite at ~200 °C. To verify the exsolution of LSCuT at extremely low temperature, SEM image of reduced LSCuT at 200 °C was shown in Fig. S4b. It should be noted that this is one of the lowest exsolution temperatures ever reported which we believe to be due to a unique combination of our highly A-site deficiency material tailoring approach and high reducing tendency of Cu ions (e.g. ΔG~-150 kJ/mol).

To understand the relationships between particle size and population and reduction temperature, we expose the LSCuT to dry H_2 atmosphere at temperature between 400 °C and 700 °C. Fig. 1b-e show the corresponding SEM images of these samples, illustrating that NPs are distributed uniformly on the perovskite surface. Particle size distribution of Cu NPs in SEM images is analyzed by using binary transferred data with image J software as shown in Fig. 1f. For the 400

°C reduced sample, small Cu NPs (< 20 nm) were exsolved (~94 particles per μm^2). The particle size decreases as the reduction temperature increased at 500 °C and further to 700 °C sample, although without showing any sign of agglomeration (particles still appear to be monomodal) and is stable over time as observed in the Fig. 1 SEM images. As shown in Fig. S5a, the average particle size of exsolved Cu NPs is ~8 nm, ~25 nm, ~30 nm and ~32 nm at 400 °C to 700 °C, respectively. The average particle size continually increases with increasing temperature, up to ~51 nm (Fig. 1f). Fig. S5b shows the amount of exsolved Cu atoms. As the temperature increases, the amount of exsolved atoms continuously increase. The results show the possibility of using Cu-based perovskite electrodes at various temperatures, having tailorable particles size and population.

The morphological characteristics and elemental distribution of reduced LSCuT at 600 °C were examined by TEM and EDS (Fig. S6). To demonstrate compositional distribution of NPs and substrate, EDS elemental mapping was also conducted. The results show that La, Sr, Ti, and O are distributed homogeneously, and the segregation of Cu is observed clearly, indicating that Cu cations are exsolved. The Cu NPs (30~40 nm diameter) appeared to be well attached to the substrate. Most of Cu cations are still present in the perovskite due to exsolution at relatively low temperature (600 °C for 12 h).
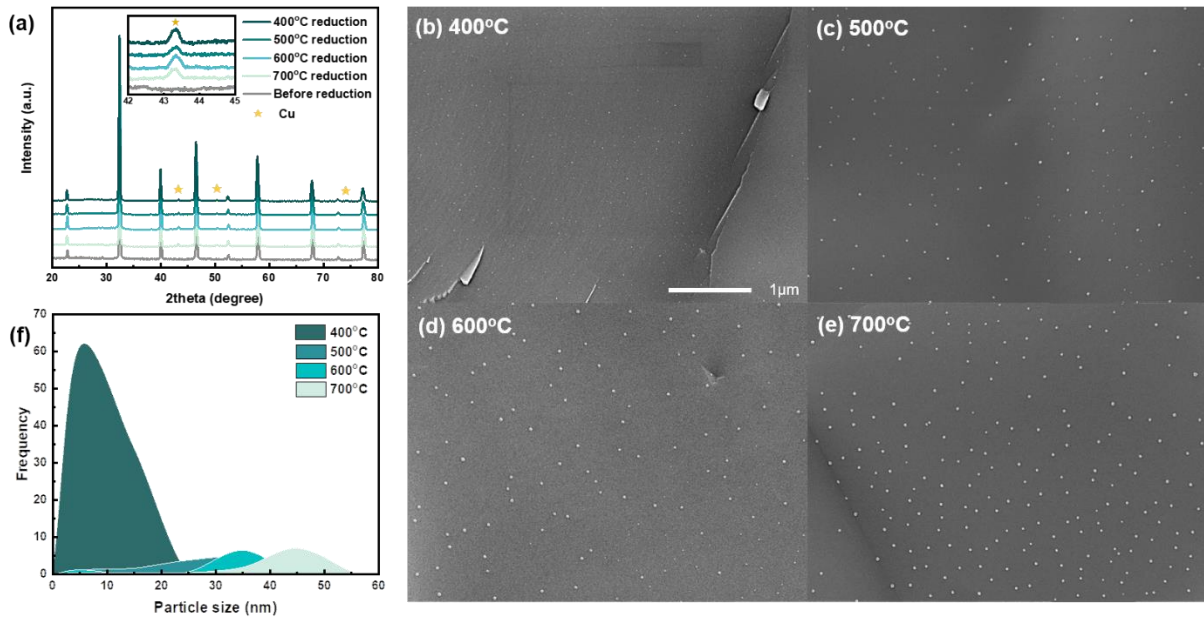
Figure 1. (a) X-ray diffraction (XRD) patterns of before and after reduction of LSCuT perovskite. (b-e) SEM image of the exsolved Cu NPs of LSCuT at different reduction temperatures between 400 °C and 700 °C in a condition of dry H_2 atmosphere for 12 h. (f) the particle size distribution and frequency of exsolved Cu particles by using ImageJ program.

We measured the relationship between reduction time and exsolution phenomenon by exposing the LSCuT samples to dry H_2 atmosphere at 600 °C. Fig. 2a-d shows the SEM images of the exsolved LSCuT for various reduction times (0 h, 12 h, 24 h and 36 h). For all the reduced samples, Cu NPs are uniformly distributed on the surface (Fig. 2b-d). Population density, exsolved Cu atoms and frequency are analyzed by using binarized SEM micrographs analyzed by image J software (Fig. 2e). Fig. 2e shows the particle size distribution of Cu NPs in SEM images according to the reduction time. Over the reduction time, nucleation continues and produce smaller particles, which reduces the average particle size. As shown in Fig. 2f, g, population density and exsolved Cu atoms

increase because the nucleation occurs as increase the reduction time increases. These enlarged active sites on the surface can effectively improve catalytic activity. These results can be described by nucleation theory[41,42]. The exsolution phenomenon can still occur at 400 °C because of a presence of a strong driving force which is the exposure to low PO_2 environment ($\sim 10^{-22}$ atm). At relatively low temperature (400 °C), nucleation is more dominant as compared to particle growth. Therefore, 400 °C sample has smaller particles and high population density (fig. 1). On the contrary, 500 °C sample exposures higher temperature so that the particle growth is more dominant. At 500 to 700 °C, population density increases again with increasing the temperature because of high ion diffusion rate in lattice through the bulk and surfaces as shown in Fig. 1c-e and Fig. S6. According to Tang C and Kousi, K[43], the diffusion process in exsolution phenomenon is strongly affected by temperature. Therefore, exsolved Cu NPs size is more affected by temperature than reduction time (Fig. 1f and Fig. 2e) These data confirmed that the temperature greatly affected the exsolution process and it is consistent with our data. And the results suggest that thermal agglomeration which is one of the main problems in Cu catalyst can be controlled via in-situ exsolution.
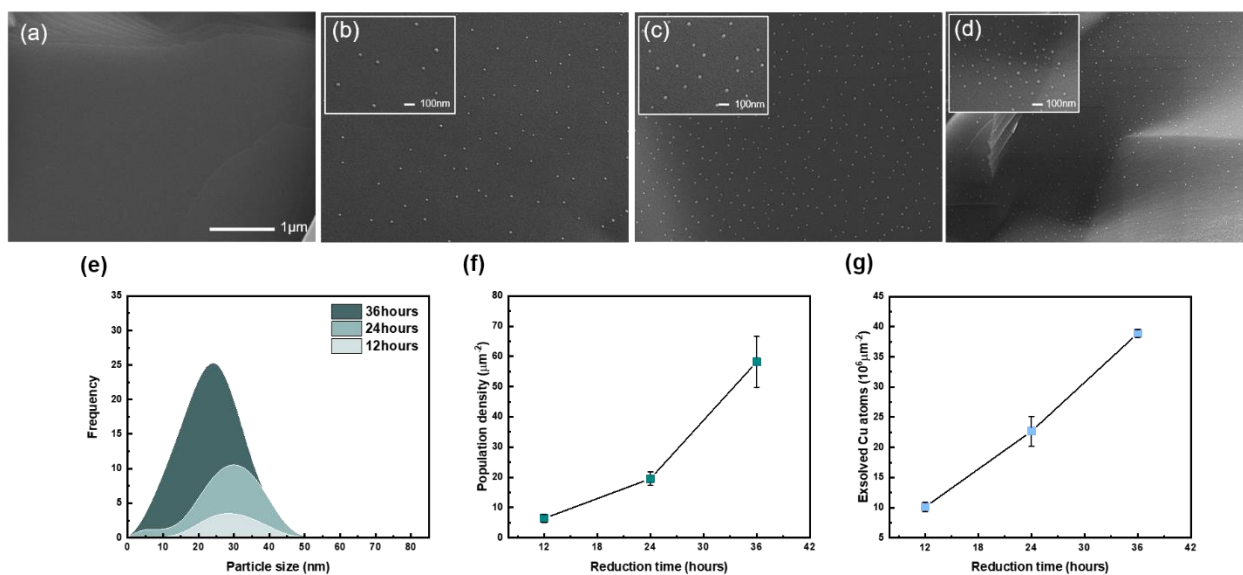
Figure 2. (a-d) SEM images of the exsolved Cu NPs of LSCuT at different reduction time of (a) fresh sample, (b) 12 hours, (c) 24 hours and (d) 36 hours in a condition of dry H_2 atmosphere at 600 °C. (d) shows population density and exsolved Cu atoms. (e-g) the particle size distribution and frequency of exsolved Cu NPs by using ImageJ program.

3.2. Thermal stability and electrocatalytic activity of catalyst

In order to determine the thermal stability of exsolved Cu particles, we compare them to infiltrated particles (Fig. 3). For a proper comparison, both materials were designed to have a porous electrode structure and to have the same equivalent metal loading (12 mol% Cu loading in LST which is equivalent to doped Cu in LSCuT). The infiltrated NPs are initially uniformly distributed, with small size NPs because of the urea decomposition synthetic method[44], but they coalesce rapidly over 48 h. Due to the high mobility of Cu NPs and weak interaction between Cu NP and LST scaffold, deposited Cu NPs redeploy even on the cross-section area which did not have particles initially (Fig. 3a). In direct contrast, for LSCuT, the population density increases with time, maintaining small particle size distribution even after prolonged reduction time. Therefore, in- situ exsolution is an effective way for preparing Cu NPs on perovskite substrate preventing thermal agglomeration. Fig. 3c shows the population density and average particle size of infiltrated and exsolved particles. It is apparent that the particle population of the infiltrated samples decreases with increasing reduction time because deposited Cu NPs have a relatively weak interaction with substrate which allows for thermal agglomeration to proceed[8]. However, exsolved particles are not only uniformly distributed but also have high population density. The population continuously increases, remaining at very small size, ~20 nm (average particle size is 18 nm at 48 h reduction) which corresponds to the tendency of bulk LSCuT samples (Fig. 2). Exsolved Cu

particles have higher interaction with substrate such that they display no agglomeration even at high temperature, under the investigated conditions[27,45]. Until now, many other studies have been unable to avoid the agglomeration and migration of Cu in high operating temperature [31,46,47] However, we identify exsolution is a promising way to fabricate thermally stable Cu catalyst for SOFC application.
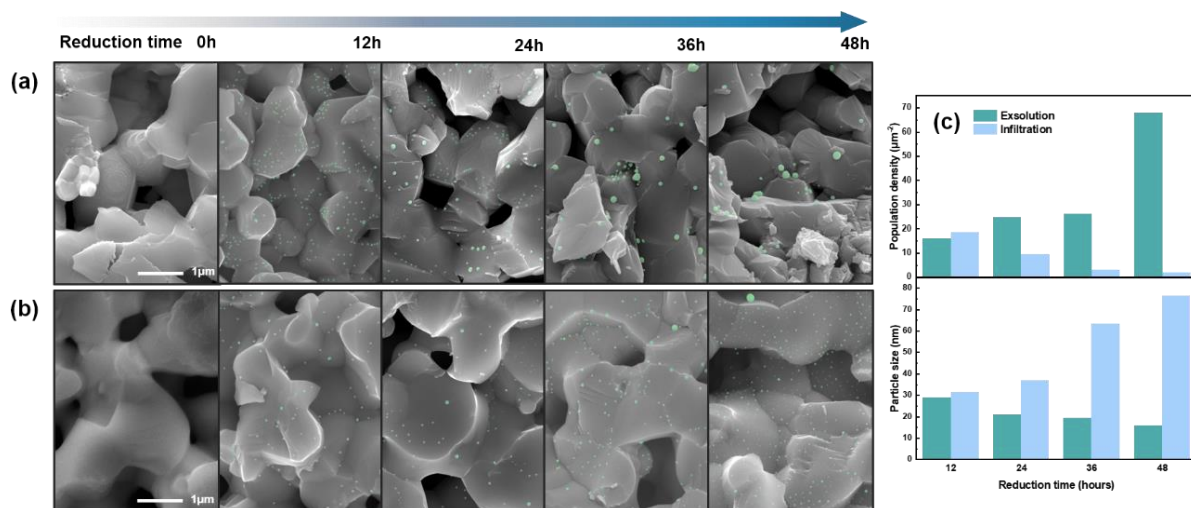

Figure 3. SEM image of (a) infiltrated and (b) exsolved Cu NPs in dry H_2 at 600 ℃ for 12 h, 24 h, 36 h and 48 h. (Cu particles are highlighted in blue in SEM image.) Population density and particle size as function of reduction time of (c) LSCuT exsolution and Cu infiltration sample.

Fig. 4a shows schematic illustration of electrochemical reduction (ER) in single cell by applying 2.3 volts in 50% H_2O/N_2 gas atmosphere, at 900 ℃. Under this voltage-driven condition, Cu NPs are spontaneously and almost instantaneously evolved with homogeneous structure, as in Cu^{2+} to Cu^0 [18]. Fig. 4b, c show SEM image after ER only for 100 s of LSCuT and infiltrated Cu/LST anode. It demonstrates that the Cu NPs were exsolved under voltage (2.3 V) and the NPs size is ~10 nm, whereas infiltrated Cu NPs size is ~50 to 150 nm after ER. When the onset voltage is applied to

13

the anode, LSCuT anode is reduced producing small and richly-populated NPs on the surface even at higher temperature (900 °C) than gas reduction (600 °C). Conventional Cu-based cermet anode materials display high tendency to agglomerate[46,48,49,50], but exsolved Cu NPs with voltage-driven show good stability with homogeneous particle distribution. These differences affect the cell performance as shown in Fig. 4d, e. The impedance data of the single cell with the LSCuT and infiltrated Cu/LST measured under open circuit voltage (OCV) after ER at 900 °C (Fig. 4d). The polarization resistance (R_P), which is the difference between the intercepts in the x-axis, is attributed to the polarization of the electrodes. The LSCuT cell has the low R_P, while infiltrated Cu/LST has significant large R_P after ER (0.04 and 0.66 Ωcm^2 for LSCuT and infiltrated Cu/LST). As shown in Fig. 4e, we operated infiltrated electrode to compare with LSCuT anode with ER. OCVs of the cells are around 1.05 V, which is close to the theoretical value, indicating dense structure of electrolyte (Fig. S7). LSCuT showed much higher performance (1.38 Wcm^{-2}) than infiltrated Cu/LST (0.57 Wcm^{-2}), even though the Cu/LST was deposited with the same amount of Cu in LSCuT (~5 wt%). The detailed parameters are shown in Fig. 4f. Average particle size and population density of LSCuT were ~9 nm and 111 particles μm^{-2}, respectively. However, infiltrated Cu/LST sample were ~53 nm and 7 particles μm^{-2}, respectively. ER process produces numerous NPs on the surface, leading to superior electrochemical performance. These results of excellent catalytic properties and stability with exsolved Cu NPs demonstrate the outstanding performance capabilities achievable with emergent electrochemical reduction.
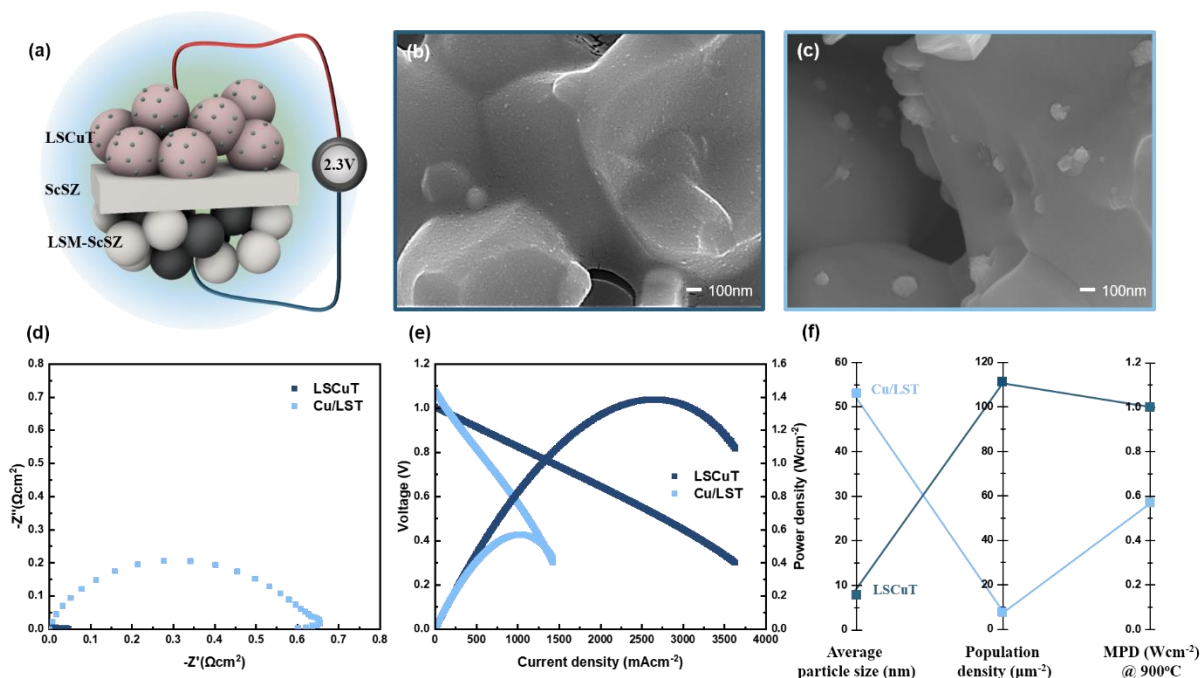
Figure 4. (a) Schematic illustration of electrochemical reduction process in single cell. SEM image of (b) LSCuT, (c) infiltrated Cu/LST electrodes after ER. (d) electrode polarization and (e) I-V-P curved for the LSCuT and infiltrated Cu/LST single cell after ER (900 ℃). (f) Comparison of average particle size, population density and maximum power density (MPD) of LSCuT and infiltrated Cu/LST.

Fig. 5a displays EIS of LSCuT‖ScSZ‖LSM-ScSZ single cell at various temperatures (900 to 600 ℃) after ER. Both ohmic resistance (R_Ω) and R_P increased as temperature decreased, which means that the charge transfer is affected by the temperature. R_p of LSCuT in 3 % H_2O/H_2 at 900, 800, 700 and 600 ℃ are 0.04, 0.11, 0.33 and 1.58 Ωcm^2, respectively, demonstrating comparable electrochemical performance even though we use Cu, which has relatively lower catalytic activity than other transition metals. R_Ω, which is the intercepts of the semicircles in high frequency region on the x-axis, is associated with the ScSZ electrolyte. R_Ω of the single cell are about 0.13, 0.16,

15

0.23 and 0.49 Ωcm^2, at 900 to 600 °C respectively, which show good agreement with observed thickness of ScSZ support (90 μm). As shown in Fig. 5b, MPDs at each temperature are displayed. The MPDs of 1.38, 1.04, 0.57 and 0.20 Wcm^{-2} are achieved at 900 to 600 °C, respectively, which suggest the excellent output for electrolyte-supported full cell with small amount of Cu catalyst content in anode. The high MPD of the cell with LSCuT anode is attributed to the enough active sites of exsolved NPs (Fig. 4a). Fig. S7 clearly shows the good contact between cathode, anode and electrolyte. No delamination was observed in the interface after ER. Long-term stability of the single cell with LSCuT anode was conducted at 900 °C under constant current of 1500 $mAcm^{-2}$ in 3 % H_2O/H_2. As shown in fig. 5c, the single cell shows highly stable potential (~0.7 V) for 150 h with negligible degradation, suggesting good stability of the LSCuT anode under high temperature operating conditions. Fig. 5d and table S1 show the cell performance with various anode materials. The achieved maximum power density of the electrolyte-supported single cell, with LSCuT anode, has higher performance than most of the Cu-based electrolyte-supported single cells[51,52,53,54,55,56,57,58]. Compared to Cu-based cermet anodes[49,57,50,58], the LSCuT anode has superior electrochemical performance, considering the amount of introduced catalyst (cermet vs Cu-doped perovskite). Compared to Cu exsolved $YST_{1-x}Cu_x$[52], $(LaSr)_{0.9}Fe_{0.9}Cu_{0.1}O_{4-\delta}$ (LSFCu)[53] $La_{0.5}Sr_{0.5}Fe_{0.8}Cu_{0.15}Nb_{0.05}O_{3-\delta}$ (LSFCNb)[54] and Fe-Cu exsolved $La_{0.5}Sr_{0.6}Fe_{0.8}Cu_{0.15}Nb_{0.55}O_{3-\delta}$ $(LS_{0.6}FCN)$[56], LSCuT also displays higher performance. In particular, the performance is superior to LSFCu used in combination with $Ba(Zr_{0.1}Ce_{0.7}Y_{0.2})O_{3-\delta}$ (BZCY), which has high ion conductivity. It should be noted that much higher performance can be achieved if we add ion conductor such as ScSZ (or we use 2 components electrode), which can improve the conductivity. Compared with $CuFe_2O_4$ (CFO) spinel anode[55], LSCuT has slightly higher performance. In spinel structure (AB_2O_4), A-site element (A=Cu) contributes to the catalytic activity. Nevertheless, B-

site doped perovskite structure (ABB'O$_3$, B'=Cu) has much lower amount of Cu-doping, LSCuT appears to have higher performance. These results show that Cu exsolution with synergistic effect of ER enhances electrochemical performance. The reasons that the electrochemical performance could be maximized with only a small amount of Cu doping are: First, the introduction of A-site deficiency which can help the Cu exsolution from the perovskite lattice and improve the conductivity of anode[18,59]. Second is highly active and thermally stable nanostructure with strong particle-substrate interaction. Third is the instant homogeneous nucleation of NPs on the perovskite surface via electrochemical reduction.
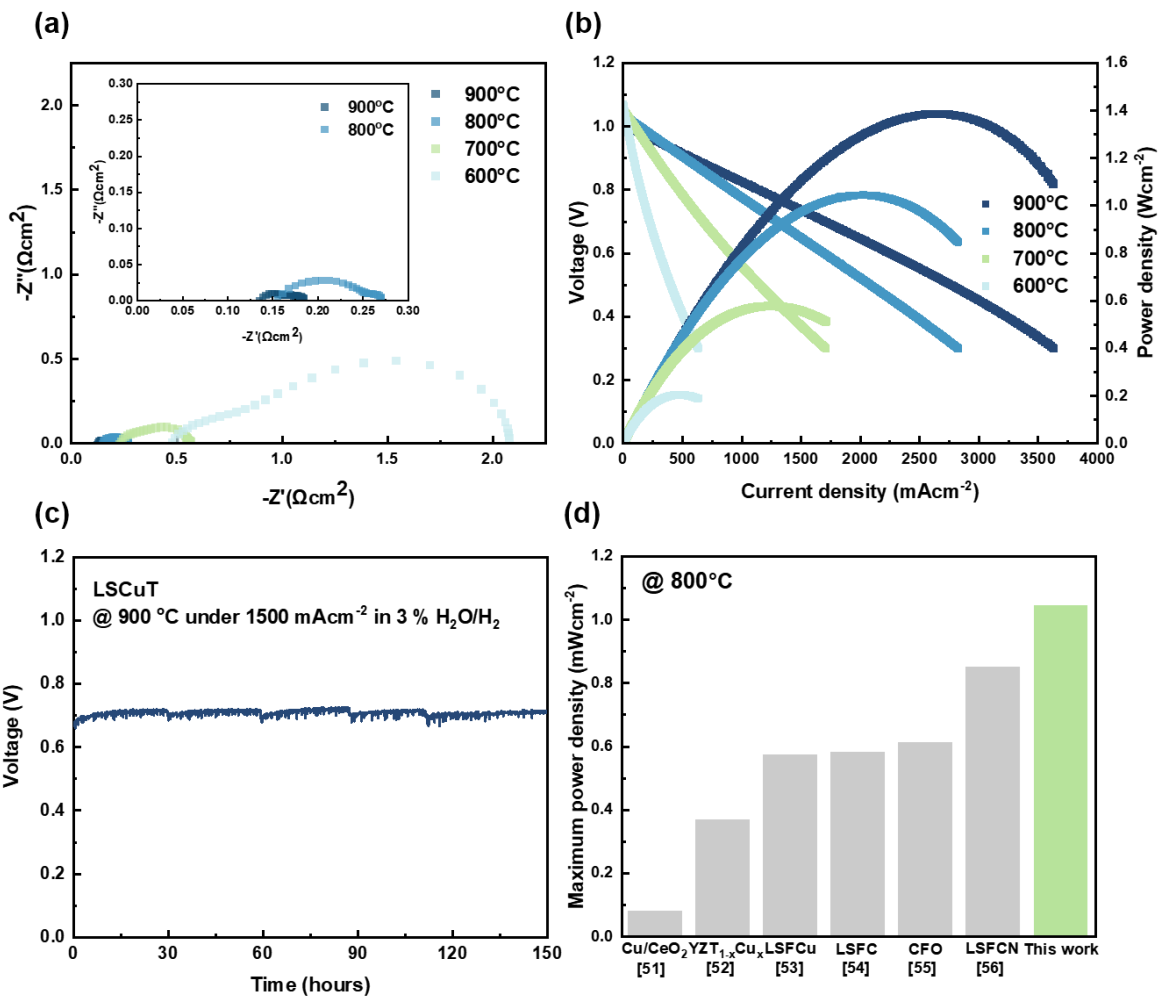
Figure 5. Electrochemical performance of LSCuT‖ScSZ‖LSM-ScSZ single cell. (a) and (b) show EIS and I-V-P curves for the LSCuT single cell fed with 3 % H_2O/H_2 with operating from 900 to 600 ℃. (c) shows the long-term stability test of the cell with LSCuT anode. (d) shows the comparison of the MPD of electrolyte-supported cells with various anode materials at 800 ℃. [51,52,53,54,55,56]

4. Conclusion

Due to high mobility of Cu, Cu based cermet suffers from degradation of performance when exposed to high temperatures (600-900 ℃). In this work, we designed and synthesized a promising new anode catalyst material and evaluated its thermal stability by comparing with infiltration process. The exsolved NPs from the $La_{0.43}Sr_{0.37}Cu_{0.12}Ti_{0.88}O_{3-\delta}$ lattice are metal Cu, which is different from the deposited Cu through infiltration process. The maximum power density of the ScSZ electrolyte-supported single cell with LSCuT anode achieves 1.38, 1.04, 0.57 and 0.20 Wcm^{-2} at 900 to 600 ℃ using 3 % H_2O/H_2 fuel, respectively. High power density is achieved using a LSCuT anode via ER with instant reduction. Our study suggests that exsolved Cu NPs have enhanced thermal stability and ER benefits the preparation of highly active anode by synergistic effect in electrochemical performance behavior. This desirable result may provide a new insight for the design of highly stable with simplified reduction process in many fields, including SOFCs, electrolysis, and so on.

18

REFERENCES

[1]   Orera, A., Slater, P. R. Chem. Mater. 22 (2010) 675-690

[2]   Damo, U. M., Ferrari, M. L., Turan, A., Massardo, A. F. Energy (2019) 235-246

[3]   Wang, W., Su, C., Wu, Y., Ran, R., Shao, Z. Chem. Rev. 113 (2013) 8104-8151

[4]   Song, B., Ruiz-trejo, E., Bertei, A., Brandon, N. P. J. Power Sources 374 (2018) 61-68

[5]   Covin, P. I., Petit, C. T. G., Lan, R., Irvine, J. T. S., Tao, S. Adv. Energy Mater. 1 (2011) 314-332

[6]   Lv, H., Lin, L., Zhang, X., Song, Y., Matsumoto, H., Zeng, C., Ta, N., Liu, W., Gao, D., Wang, G., Bao, X. Adv. Mater. 32 (2020) 1906193-1906202-

[7]   Liu, S., Liu, Q., Fu, X., Luo, J. L. Appl. Catal. B Environ. 220 (2018) 283–289

[8]   Neagu, D., Tsekouras, G., Miller, D.N., Ménard, H., Irvine, J. T. S. Nat. Chem. 5 (2013) 916-923

[9]   Zhu, J., Zhang, W., Li, Y., Yue, W., Geng, G., Yu, B. Appl. Catal. B Environ. 268 (2020) 118389-118398

[10] Yu, J., Zhang, L., Qian, J., Zhu, Z., Ni, S., Liu, G., Xu, X. *Appl. Catal. B Environ.* 256 (2019) 117818-117827

[11] Bastidas, D. M., Tao, S., Irvine, J. T. S. J. Mater. Chem. 16 (2006) 1603–1605

[12] Lakshminarayanan, N., Choi, H., Kuhn, J. N., Ozkan, U. S. Appl. Catal. B Environ. 103 (2011) 318–325

[13] Tao. S., Irvine, J. T. S. Nat. Mater. 2 (2003) 320-323

[14] Zhu, T., Troiani, H., Mogni, L. V., Santaya, M., Han, M., Barnett, S. A. J. Power Sources 439 (2019) 227077-227087

[15] Song, Y., Li, H., Xu, M., Yang, G., Wang, W., Ran, R., Zhou, W., Shao, Z. Small 16 (2020) 2001859-2001867

[16] Di Bartolomeo, E., Basoli, F., Luisetto, I., Tuti, S., Zurlo, F., Salehi, A., Licoccia, S. Appl. Catal. B Environ. 191 (2016) 1–7

[17] Neagu, D., Oh, T. S., Miller, K. N., Ménard, H., Bukhari, S. M., Gamble, S. R., Gorte, R. J., Bohs, J. M., Irvine, J. T. S. Nat. Commu. 6 (2015) 1-8

[18] Myung, J. H., Neagu, D., Miller, D. N., Irvine, J. T. S. Nat. 537 (2016) 528-531

[19] Kim, K. J., Rath, M. K., Kwak, H. H., Kim, H. j., Han, J. W., Hong, S. T., Lee, K. T. ACS Catal. 9 (2019) 1172-1182

[20] Sun, Y. F., Li, J. H., Wang, M. N., Hua, B., Li, J., Luo, J. L. *J.* Mater. Chem. A 3 (2015) 14625-14630

[21] Chung, Y. S., Kim, T., Shin, T. H., Yoon, H., Park, S., Sammes, N. M., Kim, W. B., Chung, J. S. J. Mater. Chem. A 5 (2017) 6437-6446

[22] Zhou, J., Shin, T. H., Ni, C., Shen, G., Wu, K., Cheng, Y., Irvine, J. T. Chem. Mater. 28 (2016) 2981-2993

[23] Liu, S., Chuang, K. T., Luo, J. L. ACS Catal. 6 (2016) 760-768

[24] Du, Z., Zhao, H., Yi, S., Xia, Q., Gong, Y., Zhang, Y., Cheng, X., Li, Y., Gu, L., Świerczek, K. ACS Nano 10 (2016) 8660-8669

[25] Kim, K. J., Han, H., Defferriere, T., Yoon, D., Na, S., Kim, S. J., Dayaghi, A. M., Son, J., Oh, T. S., Jang, H. M. Choi, G. M. J. Am. Chem. Soc. 141 (2019) 7509-7517

[26] Bian, L., Duan, C., Wang, L., Zhu, L., Hayre, R. O., Chou, K. C. J. Power Sources 399 (2018) 398-405

[27] Park, S., Kim, Y., Han, H., Chung, Y. S., Yoon, W., Choi, J., Kim, W. B. Appl. Catal. B Environ. 248 (2019) 147-156

[28] Chen, X., Ni, W., Wang, J., Zhong, Q., Han, M., Zhu, T. Electrochimica Acta 277 (2018) 226-234

[29] Spencer, M. S. Nature 323 (1886) 685-687

[30] Sousa, A. R. O., Araufo, A. J., Souza, G. S., Grilo, J. P., Loureiro, F. J., Fagg, D. P., Macedo,   D. A. Mater. Lett. 191 (2017) 141–144

[31] Jung, S., Lu, C., He, H., Ahn, K., Gorte, R. J., Vohs, J. M. J. Power Sources 154 (2006) 42–50

[32] Wan, J., Zhu, J. H., Goodenough, J. B. Solid State Ionics 177 (2006) 1211–1217

[33] Wu, X., Yu, Y., Chen, Y., Li, L., Ma, Z. F., Yin, Y. ACS Appl. Mater. Interfaces 12 (2020) 34890-34900

[34] Park, B. H., Choi, G. M. Solid State Ionics 262 (2014) 345–348

[35] Aljaberi, A. D., Irvine, J. T. S. J. Mater. Chem. A 1 (2013) 5868–5874

[36] Sun, Y., Li. J. H., Cui, L., Hua, B., Cui, S. H., Li, J., Juo, J. L. Nanoscale 3 (2015) 11173–11181

[37] Neagu, D., Irvine, J. T. S. Chem. Mater. 22 (2010) 5042–5053

[38] Kim, S. W., Park, M., Kim, H., Yoon, K. J., Son, J. W., Lee, J. H., Kim, B. K., Lee, J., H., Hong, J. Applied Catal. B, Environ. 200 (2017) 265–273

[39] Thieu, C. A., Park, S., Kim, H., Ji, H. I., Lee, J., Yoon, K. J., Yang, S., Son, J. W. Int. J. Energy Res. 44 (2020) 9995–10007

[40] Kim, S. J., Choi, M., Lee, J., Lee, W. J. Eur. Ceram. Soc. 40 (2020) 3089–3097

[41] Sosso, G. C., Chen, J., Cox, S. J., Fitzner, M., Pedevilla, P., Zen, A., Michaelides, A. Chem. Rev. 116 (2016) 7078-7116

[42] Gao, Y., Chen, D., Saccoccio, M., Lu, Z., Ciucci, F. *Nano Energy* 27 (2016) 499-508

[43] Tang, C., Kousi, K., Neagu, D., Portoles, J., Papaioannou, E. I., Metcalfe, I. S. Nanoscale 11 (2019) 16935-16944

[44] Yoon, K. J., Biswas, M., Kim, H. J., Park, M., Hong, J., Kim, H., Son, J. W., Lee, J. H., Kim, B. K., Lee, H. W. Nano Energy 36 (2017) 9-20

[45] Neagu, D., Kyriakou, V., Roiban, I. L., Aouine, M., Tang, C., Caravaca, A., Van De Sanden,   M. C. ACS Nano 13 (2019) 12996–13005

[46] Kiratzis, N., Holtappels, P., Hatchwell, C. E., Mogensen, M., Irvine, J. T. S. Fuel cells 1 (2001) 211–218

[47] Kaur, G., Basu, S. Int. J. Energy Res. 39 (2015) 1345–1354

[48] Benoved, N., Kesler, O. J. Power Sources 193 (2009) 454–461

[49] Solovyev, A. A., Ionov, I. V., Shipilova, A. V., Rabotkin, S. V. J. Phys. Conf. Ser. 1393 (2019) 012140-012147

[50] Li, W., Guan B., Liu, M., Wei, B., Zhu, X., Wang, Z., Lu, Z. J. Solid State Electrochem. 22 (2018) 1735–1743

[51] Sarruf, B. J. M., Hong, J. E., Steinberger-Wilckens, R., de Miranda, P. E. V. Int. J. Hydrogen Energ*y* 45 (2020) 5297-5308

[52] Qiao, J., Chen, H., Wang, Z., Sun, W., Li, H., Sun, K. Industrial & Engineering Chemistry Research 59 (2020) 13105-13112

[53] Fu, L., Zhou, J., Yang, J., Lian, Z, Wang, J., Cheng, Y., Wu, K. Appl. Surf. Sci. 511 (2020) 145525-145534

[54] Zhou, N., Yin, Y. M., Chen, Z., Song, Y., Yin, J., Zhou, K., Ma, Z. F. J. Electrochem. Soc. 165 (2018) 629-634

[55] Kang, B., Matsuda, J., Ishihara, T. *J. Mater. Chem. A* 7 (2019) 26105-26115

[56] Song, Y., Yin, Y. M., Li, L., Chen, Z., Ma, Z. F. Chem. Comm. 54 (2018) 12341-12344

[57] Zhu, L., Liu, X., Han, F., Sun, J., ki, H., Wang, H., Yu, S., Pei, L. Solid State Ionics 288 (2016) 115-119

[58] Ye, X., Wang, S. R., Hu, Q., Chen, J. Y., Wen, T. L., Wen, A. Y. Solid State Ionics 180 (2009) 276-281

[59] Zhu, T., Troiani, H. E., Mogni, L. V., Han, M., Barnett, S. A. Joule 2 (2018) 478–496